JGR Space Physics

RESEARCH ARTICLE
10.1029/2020JA028768

Key Points:

- Effect of a solar wind dynamic pressure front on the open-closed polar cap boundary
- Determination of the magnetic reconnection rate for a southward interplanetary magnetic field case
- Response of the dayside/nightside reconnection rate to a solar wind dynamic pressure front

Correspondence to:
A. Boudouridis,
thanasis@spacescience.org

Citation:
Boudouridis, A., Connor, H. K., Lummerzheim, D., Ridley, A. J., & Zesta, E. (2021). Changes in the magnetic field topology and the dayside/nightside reconnection rates in response to a solar wind dynamic pressure front: A case study. *Journal of Geophysical Research: Space Physics*, *126*, e2020JA028768. https://doi.org/10.1029/2020JA028768

Received 30 SEP 2020
Accepted 4 JUN 2021

Changes in the Magnetic Field Topology and the Dayside/Nightside Reconnection Rates in Response to a Solar Wind Dynamic Pressure Front: A Case Study

A. Boudouridis[1,2,3], H. K. Connor[4], D. Lummerzheim[4], A. J. Ridley[5], and E. Zesta[6]

[1]Space Sciences Institute, Boulder, CO, USA, [2]Cooperative Institute for Research in Environmental Sciences, University of Colorado, Boulder, CO, USA, [3]National Center for Environmental Information, National Oceanic and Atmospheric Administration, Boulder, CO, USA, [4]Geophysical Institute, University of Alaska, Fairbanks, AK, USA, [5]University of Michigan, Ann Arbor, MI, USA, [6]NASA Goddard Space Flight Center, Greenbelt, MD, USA

Abstract One of the most significant observations associated with a sharp enhancement in solar wind dynamic pressure, P_{SW}, is the poleward expansion of the auroral oval and the closing of the polar cap. The polar cap shrinking over a wide range of magnetic local times (MLTs), in connection with an observed increase in ionospheric convection and the transpolar potential, led to the conclusion that the nightside reconnection rate is significantly enhanced after a pressure front impact. However, this enhanced tail reconnection has never been directly measured. We demonstrate the effect of a solar wind dynamic pressure front on the polar cap closure, and for the first time, measure the enhanced reconnection rate in the magnetotail, for a case occurring during southward background Interplanetary Magnetic Field (IMF) conditions. We use Polar Ultra-Violet Imager (UVI) measurements to detect the location of the open-closed field line boundary, and combine them with Assimilative Mapping of Ionospheric Electrodynamics (AMIE) potentials to calculate the ionospheric electric field along the polar cap boundary, and thus evaluate the variation of the dayside/nightside reconnection rates. We find a strong response of the polar cap boundary at all available MLTs, exhibiting a significant reduction of the open flux content. We also observe an immediate response of the dayside reconnection rate, plus a phased response, delayed by ~15–20 min, of the nightside reconnection rate. Finally, we provide comparison of the observations with the results of the Open Geospace General Circulation Model (OpenGGCM), elucidating significant agreements and disagreements.

Plain Language Summary This study provides valuable information on how the Earth's magnetosphere (the magnetized protective bubble around the Earth) is eroded by powerful explosions at the Sun. The response of the polar cap size and the reconnection rates in the magnetosphere to a solar wind high density front are investigated for an event with Interplanetary Magnetic Field orientation anti-parallel to the Earth's magnetic field. We make a data-based assessment, using Polar spacecraft ultraviolet images and assimilative model-generated potentials, plus a model-based comparison using a global magnetospheric model. An immediate response is observed at the dayside ionosphere for both the polar cap boundary and the reconnection rate mapped to the ionosphere. We also observe about 15–20 min delayed effect on various sectors of the nightside ionosphere. The comparison with the model reveals considerable discrepancies on the dayside ionosphere and significant agreements at the nightside ionosphere.

1. Introduction

Changes of the Earth's magnetic field topology drive magnetospheric activity. The dominant mechanism by which such changes are imparted on the terrestrial system, and by which mass, energy, and momentum flow from the solar wind to Earth's environment is magnetic reconnection (e.g., Fuselier & Lewis, 2011; Paschmann et al., 2013). The balance or not of reconnection rates on the dayside and nightside magnetosphere controls the field topology and the state of the system.

The Interplanetary Magnetic Field (IMF) is undeniably the most important solar wind driver of magnetic reconnection and magnetospheric activity. Its crucial role has been long documented (e.g., Akasofu, 1980; Boyle et al., 1997; Cowley, 1984; Rich & Hairston, 1994). In the past two decades, another solar wind driver

has emerged as a significant contributor to the activity in the terrestrial magnetosphere. Multiple studies have shown that sharp enhancements in solar wind dynamic pressure, P_{SW}, have profound effects on the terrestrial magnetosphere-ionosphere system (e.g., Boudouridis et al., 2003; Liou, 2006). Significant changes in ionospheric convection (Boudouridis et al., 2005, 2007, 2011; Boudouridis, Zesta, Lyons, & Anderson, 2004; Boudouridis, Zesta, et al., 2008; Connor et al., 2014), auroral particle precipitation and changes in the size of the polar cap (Boudouridis et al., 2003, 2005; Boudouridis, Zesta, Lyons, Anderson, & Lummerzheim, 2004; Chua et al., 2001; Holmes et al., 2014), and enhancement of field-aligned currents (e.g., Ozturk et al., 2018; Zesta et al., 2000) are major effects induced by the impact of solar wind dynamic pressure fronts.

The most striking magnetospheric response to a solar wind pressure enhancement has been shown to be the shrinking of the polar cap, and therefore the decrease in the amount of the open magnetic flux in the system. This observation is particularly unexpected for cases with steady southward IMF conditions, during which the polar cap is supposed to have its greatest extent, encompassing a large amount of open flux (Boudouridis et al., 2003, 2005; Boudouridis, Zesta, Lyons, Anderson, & Lummerzheim, 2004; Zesta et al., 2000). The poleward motion of the polar cap boundary varies with magnetic local time (MLT), being more evident at the nightside and flanks (where it can reach up to 10° of magnetic latitude (MLAT) in some cases), but also occasionally present on the dayside due to a combination of highly southward IMF conditions and enhanced ionospheric convection (Boudouridis, Zesta, Lyons, Anderson, & Lummerzheim, 2004). Boudouridis et al. (2003) have argued that the amount and MLT extent of the polar cap closing depends on the "preconditioning" of the magnetosphere, referring to the energy load of the magnetosphere in the time preceding the sudden compression by the solar wind pressure front. This effect was studied extensively by Boudouridis et al. (2003, 2005); Boudouridis, Zesta, Lyons, Anderson, & Lummerzheim (2004) using Defense Meteorological Satellite Program (DMSP) precipitating particle measurements.

Boudouridis, Zesta, Lyons, Anderson, & Lummerzheim (2004) compared the polar cap size response to pressure fronts for two event categories, strong southward IMF and near-zero IMF B_z conditions prior to the front impact time. They observed an extensive shrinking of the polar cap at a wide MLT range (well into the dayside) during the highly negative preexisting IMF B_z events. In contrast, they saw a more moderate poleward motion of the polar cap boundary, mainly confined to the nightside, when the preexisting IMF B_z was closer to zero. Boudouridis, Zesta, Lyons, Anderson, & Lummerzheim (2004) concluded that this behavior is a result of the different amount of open flux already present in the magnetotail at the time of impact, more for negative than near-zero IMF B_z conditions. The high-pressure regime compresses the magnetotail, which responds in a stronger manner when loaded with magnetic flux. Based on these observations, Boudouridis, Zesta, Lyons, Anderson, & Lummerzheim (2004) postulated that an enhancement of the tail reconnection rate is occurring shortly after the pressure front impact. The deduced enhanced tail reconnection rate is larger during periods of strong southward IMF when the magnetotail is full of stored open flux, compared to near-zero IMF B_z cases when a smaller open flux amount is present.

In addition to DMSP particle data, the shrinking of the polar cap after a solar wind pressure enhancement has also been observed in global auroral images (Boudouridis, Lyons, et al., 2008; Hubert, Palmroth, et al., 2006; Hubert et al., 2009; Lyons, 2000; Milan et al., 2004; Zesta et al., 2000). In all these studies the auroral oval expands poleward and intensifies while the polar cap is significantly reduced in size. The reduction is observed mostly on the nightside. Boudouridis, Lyons, et al. (2008) used Polar spacecraft Ultra-Violet Imager (UVI) images to evaluate the motion of the polar cap boundary during an event with two characteristic pressure peaks. Their results show a high degree of correlation between the poleward expansion of the auroral oval, and the temporal profile of the solar wind dynamic pressure enhancement, after each pressure peak. This correlation is particularly striking in the 2–4 MLT sector, but also visible in other nightside MLT sectors.

As mentioned above, the reduction in the size of the polar cap means a reduction in the amount of the open flux in the magnetosphere. Since this is observed mostly on the nightside, it suggests an increase in the rate of magnetotail reconnection after sudden increases in dynamic pressure (Boudouridis, Zesta, Lyons, Anderson, & Lummerzheim, 2004; Boudouridis et al., 2003, 2005), which implies a large-scale reconfiguration of the magnetosphere. In a study by Hubert, Palmroth, et al. (2006) using Super Dual Auroral Radar Network (SuperDARN) observations, the tail reconnection potential is calculated for two consecutive pressure front impacts. The tail potential increased from ~30 and ~20 kV before, to 132 and 114 kV after the pressure

jump, respectively, pointing to a huge enhancement of the reconnection rate in the magnetotail. A study by Milan et al. (2004) found that the sudden compression of the magnetosphere due to a pressure front impact resulted in a decrease of the open flux content of the Northern Hemisphere from 0.5 to 0.2 GWb. The pre-impact value corresponds to 7%–8% of the total hemispheric flux, while the post-front value is down to only 2.5% of the total hemispheric flux, again a tremendous change signifying highly enhanced tail reconnection. The associated tail reconnection potential was estimated to be 150 kV.

The above studies show that the shrinking of the polar cap after a sudden enhancement in P_{SW} is a recurring feature, most significant during periods of strong southward IMF conditions, which makes it even more intriguing, as such reduction in open flux is not expected during these times. Based on these observations, and supportive measurements of enhancements in ionospheric convection and the transpolar potential (Boudouridis et al., 2005, 2007, 2011; Boudouridis, Zesta, Lyons, & Anderson, 2004; Boudouridis, Zesta, et al., 2008; Connor et al., 2014; Hubert, Palmroth, et al., 2006), it was surmised that the pressure front impact induces an enhancement of the nightside reconnection rate. However, this enhanced tail reconnection rate was never explicitly measured in the past as a function of MLT. For the first time, we present direct measurements of an enhancement in the magnetotail reconnection rate after a solar wind dynamic pressure front impact, for a case with southward IMF orientation.

2. Polar Cap Boundary Response

In this section we describe the quantitative criteria we use to identify the polar cap boundary location from Polar UVI auroral emissions. We demonstrate the use of these criteria by presenting the response of the polar cap boundary to a pressure front. Finally, we compare the UVI observed response to the response seen in the Open Geospace General Circulation Model (OpenGGCM) global magnetohydrodynamic (MHD) simulation, coupled with the Coupled Thermosphere Ionosphere Model (CTIM).

2.1. UVI Polar Cap Boundary Identification

Boudouridis, Lyons, et al. (2008) have pointed out that past literature, comparing DMSP precipitating particle boundaries and Ultra-Violet (UV) emission boundaries, has supported the idea of a UV-image derived open-closed field line boundary (OCB) (Baker et al., 2000; Carbary et al., 2003; Kauristie et al., 1999). We follow the statistical study of Baker et al. (2000) who demonstrated that the poleward auroral boundary derived from Polar spacecraft UVI images is a good indicator of the location of the OCB. Their study involved comparison with the DMSP-based discrete aurora poleward boundary, believed to be the best estimate of the OCB (Newell et al., 1996). They showed that, in the evening sector, the average UVI-derived poleward auroral boundary lies only ∼1° MLAT poleward of the DMSP-derived boundary. Baker et al. (2000) discussed two techniques for the identification of the OCB based on Polar UVI images, the threshold technique and the ratio technique. The first sets a constant limit of flux for the boundary, while the second one uses a constant ratio to the specific MLT sector maximum of the auroral luminosity. They went on to argue that the ratio technique, with ratios of 0.2–0.3, is the most appropriate technique to locate the OCB, based on the DMSP discrete aurora poleward boundary comparison.

There are a few additional caveats of the Polar UVI boundary identification we need to discuss. First of all, the Polar satellite suffers from a well-known "wobble" along one of the camera axes, which rotates with the orbit precession and is thus different every year. This introduces a random uncertainty in the boundary location which Brittnacher et al. (1999) estimated to be about 1.5°. Second, the Baker et al. (2000) study used the UVI data from one winter month (January 1997) when the dayglow was low. Dayglow contamination can be a serious issue during the summer months. However, Lummerzheim et al. (1997) have demonstrated that the auroral contribution in the UVI images can be extracted from the underlying dayglow even when the dayglow is the major contribution to the pixel count rate. Third, Carbary et al. (2003), based on a two-year DMSP/UVI boundary comparisons, pointed out that there are systematic errors of up to 4° in MLAT between DMSP and UVI poleward auroral boundaries, which are MLT dependent. Their maximum systematic error, however, occurs near 05 MLT, where very few DMSP orbits exist. For the rest of the oval the errors are about 1° MLAT.

2.2. OpenGGCM-CTIM Modeling

The OpenGGCM-CTIM model provides a global simulation of the response of the magnetosphere-ionosphere-thermosphere system to solar wind input. The model has been used and discussed in detail in a number of studies of the solar wind-magnetosphere-ionosphere-thermosphere interaction (e.g., Raeder, 2006; Raeder, McPherron, et al., 2001; Raeder, Wang, et al., 2001). The OpenGGCM model has been developed and continuously improved over the past two decades, and it has been extensively compared with magnetospheric and ionospheric measurements (e.g., Pulkkinen et al., 2013). Numerical details are discussed in Raeder (2003). Most relevant to this study, the OpenGGCM model has been used for studies of interplanetary shocks impacting the magnetosphere (Connor et al., 2014; Oliveira & Raeder, 2014, 2015).

The OpenGGCM is a global magnetosphere-ionosphere model that solves the resistive MHD equations with current driven instability on a non-uniform Cartesian grid (Raeder, 2003; Raeder et al., 2008). The solar wind and IMF conditions are input, and the plasma parameters and electromagnetic fields are output. Its simulation domain is 20–30 R_E upstream, several hundred to thousands of R_E downstream, and ±40–50 R_E in the YZ plane. The OpenGGCM has its inner magnetosphere boundary at 2.5–3.5 R_E where the MHD physics is no longer applicable. OpenGGCM considers the ionosphere as a 2D plane with a fixed altitude at ∼110 km. CTIM is a three-dimensional ionosphere-thermosphere model developed by the National Oceanic and Atmospheric Administration group (Fuller-Rowell et al., 1996). It self-consistently solves the neutral and ion dynamics with solar radiation, tidal modes, high-latitude electric fields, and aurora precipitation as inputs. Its simulation domain is from 80 km to several hundred km altitude for the thermosphere, and from 80 km to several thousands km altitude for the ionosphere, in geographic coordinates (Codrescu et al., 2012).

The OpenGGCM-CTIM couples the magnetosphere and upper atmosphere system by solving a current continuity equation (Kelley, 1989; Vasyliunas, 1970), assuming that the field-aligned currents close in the ionosphere. OpenGGCM provides field-aligned currents and aurora precipitation using the plasma parameters at the inner magnetospheric boundaries. The empirical equations of Kennel and Petcheck (1966), Knight (1973), and Lyons et al. (1979) are used to provide the mean energy and energy flux of the diffuse and discrete aurora precipitation. CTIM calculates the altitudinal profiles of aurora energy deposition, electron density, and conductivities using its thermosphere and ionosphere parameters with the OpenGGCM aurora input. As a result, CTIM provides realistic calculation of height integrated conductance, not depending on the widely used empirical conductance model of Robinson et al. (1987), the default conductance module of the stand-alone OpenGGCM model. The OpenGGCM field-aligned currents and the CTIM conductance calculated from the OpenGGCM aurora are used to calculate ionospheric electric potentials and thus connect the field-aligned currents to the ionospheric currents. The resulting ionospheric electric fields are used to drive the upper atmosphere system in the CTIM and the plasma flow at the OpenGGCM inner magnetosphere boundary. Connor et al. (2016) and Raeder, Wang, et al. (2001) reported that the OpenGGCM-CTIM produces more realistic behavior in the ionospheric electrodynamics, and the high-latitude thermospheric mass densities during space weather events.

In this study, the OpenGGCM OCB is calculated by tracing magnetic field lines from the ionosphere through the magnetosphere to determine if they are open or closed (Connor et al., 2014). The X range of the simulation box is (−1,000, 21) R_E, and the Y/Z ranges are (−48, 48) R_E, all in Geocentric Solar Ecliptic (GSE) coordinates. Field lines are traced from every point of a 3° magnetic longitude by 0.5° MLAT grid. The field line tracing stops when the total length of field line becomes 1,000 R_E. If the end point of the field line is located inside a 4 R_E radius in the YZ plane, the field line is closed. If this point hits the OpenGGCM's simulation box or ends up somewhere outside the 4 R_E radius the field line is considered open.

2.3. February 11, 2000 Pressure Front OCB Response

The left plot of Figure 1 shows the UVI polar cap boundary response for a pressure enhancement at 2356 UT on February 11, 2000. The bottom three panels plot propagated Wind spacecraft measurements of P_{SW}, IMF B_z, and IMF B_y. The solar wind/IMF data are propagated to (17,0,0) R_E Geocentric Solar Magnetospheric (GSM) coordinates, using the Weimer et al. (2003)/Weimer (2004) minimum variance technique, and are

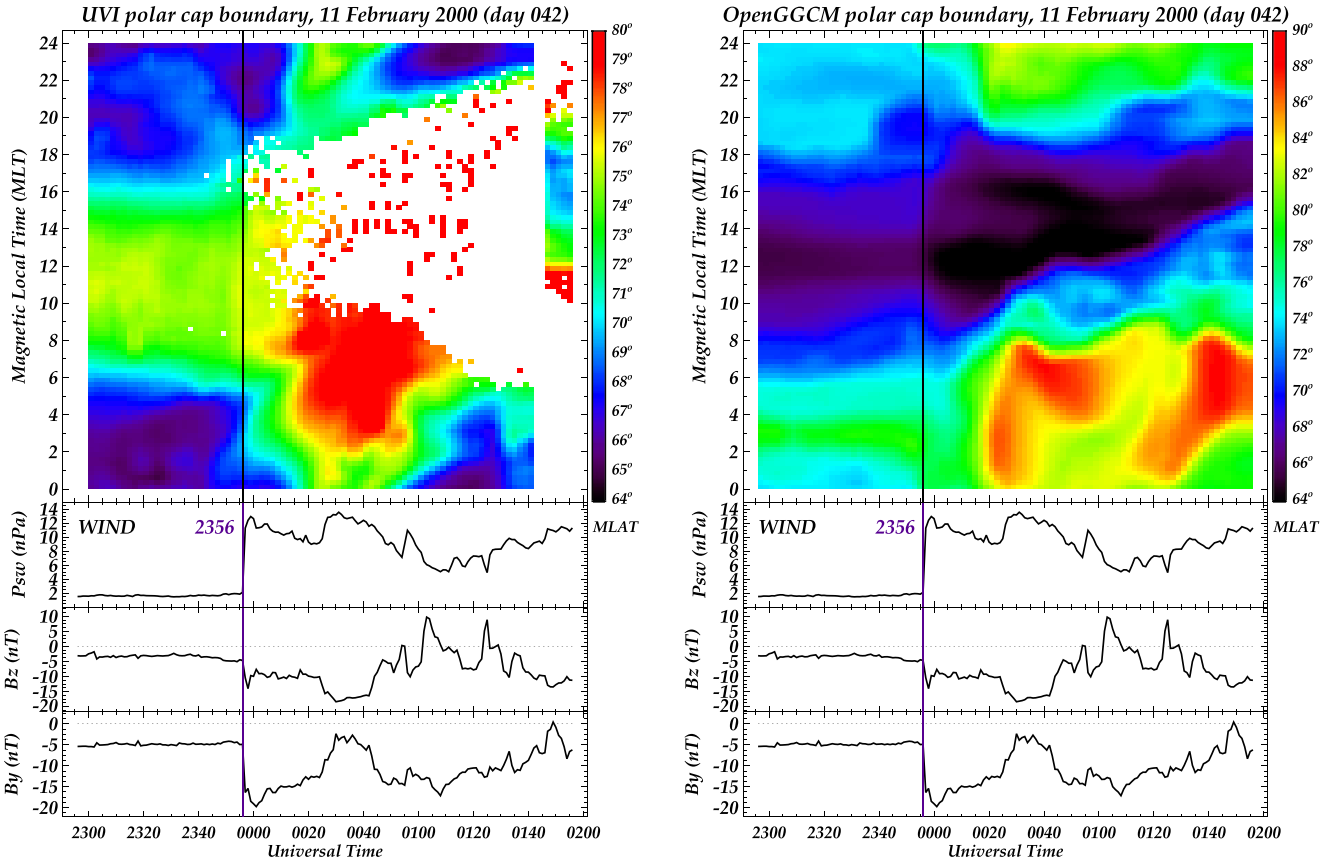

Figure 1. (left) Polar Ultra-Violet Imager (UVI)-determined polar cap boundary (color coded, top panel) as a function of time and magnetic local time (MLT) for February 11, 2000. The bottom three panels show propagated Wind P_{SW}, Interplanetary Magnetic Field (IMF) B_z, and IMF B_y observations. The vertical line marks the pressure front impact at 2356 UT. (right) Similar format plot of the Open Geospace General Circulation Model (OpenGGCM)-determined polar cap boundary (notice the different MLAT color scales).

given with 1 min resolution (Weygand & McPherron, 2006a; 2006b). The 17 R_E upstream distance is chosen because it is just outside the nominal position of the nose of the bow shock. P_{SW} jumped from 2 nPa before to 10–14 nPa after the pressure increase, where it remained for about an hour before dropping to more moderate levels of 6–10 nPa, but still elevated compared to its value before the front impact. At impact, IMF B_z changed from southward −5 nT to even more southward, initially down to −10 nT and then < −15 nT during the first hour after the pressure step, before returning to fluctuating north-south values 1 h after the P_{SW} increase. IMF B_y was also about −5 nT before, turning to −15 nT for ∼25 min, then back to −5 nT for another 20 min, before settling to values between −10 and −15 nT for the next hour.

For our case study we use the ratio technique with a value of 0.2 of the maximum UVI intensity within 15 min wide MLT sectors. The high MLT resolution provides a detailed picture of the boundary motion after the pressure enhancement. An additional feature we employed in this identification is the subtraction of a 0.4 mW/m^2 noise level emissions prior to the application of the ratio technique.

The top panel on the left shows the evolution of the polar cap boundary MLAT for all MLTs with available data (color coded in MLAT according to the color scale on the right, white indicating missing data). We use 2 min time resolution and thus average the boundaries from all UVI images within each 2 min time bin. The boundary shows a clear response to the incoming pressure front, moving to higher MLAT values at all MLTs with good measurements before and after the pressure front impact. The closing of the polar cap is more evident at dawn (02–06 MLT) where the boundary moves from about 66° to near 80° MLAT, a tremendous change. In the early morning (06–10 MLT) the boundary moves from about 74–76° to in excess of 78° MLAT, while it exhibits a motion of a couple of degrees around noon, despite the sparse data available. In the near-midnight MLT region (20–02 MLT) the increase in MLAT is from 66–68° to 74–76°. The observed

polar cap boundary motion occurs within 15 min of the front impact, first at the dayside and a bit later at the near-midnight region. The closing of the polar cap is quite dramatic, and it occurs despite the fact that the IMF B_z turned very southward at the same time, demonstrating clearly the strong effect of the magnetospheric compression on the amount of open flux in the system. It shows that a sudden P_{SW} enhancement can overwhelm and reverse the opening of the polar cap expected for further southward turning of the IMF.

The right plot of Figure 1 shows the OpenGGCM OCB response for the February 11, 2000 pressure front in the same format as in the UVI plot (notice the different MLAT color scales). The OpenGGCM boundary was averaged within 15 min MLT and 2 min UT bins for consistency with the UVI plot. There are differences and similarities between the model and data. The model has reversed boundary locations at day and night compared with the observations before the front impact. The dayside boundary (06–18 MLT) is located around 66°–70°, while the nightside boundary (18–06 MLT) is at ~72°–80°. After impact the dayside OCB moves slightly equatorward for the first 15–20 min before moving poleward in all but the 12–17 MLT sectors. By 0040 UT the noon boundary also starts moving poleward. Later times see only a progressively narrower afternoon region remaining at low MLAT. Even though there are scarce observations on the dayside, the initial model OCB motion seems to contradict the UVI OCB motion, which moves slightly poleward. At the nightside, the OCB moves significantly poleward within ~20 min from the front impact, reaching higher than 84° MLAT in the post-midnight sector (00–06 MLT), and around 80°–84° MLAT in the pre-midnight sector (18–24 MLT). This motion matches qualitatively the observed UVI boundary motion, albeit with much higher MLAT values.

3. Dayside/Nightside Reconnection Rate Response

We now turn our attention to the dayside and nightside reconnection rates before and after the solar wind dynamic pressure front at 2356 UT on February 11, 2000. We show reconnection rate estimations using AMIE potential results and Polar UVI OCB observations. We then compare the observation-based results with the OpenGGCM simulation results of the same event using the model-produced boundary and ionospheric potentials.

3.1. Reconnection Rate Determination

The AMIE technique (Richmond & Kamide, 1988) is an assimilative technique that uses least squares fitting of a variety of observations from different platforms (ground magnetometers, DMSP satellites, and SuperDARN radars), in an effort to estimate a number of ionospheric parameters, including the high-latitude potential distribution, ionospheric electric field, hemispheric power, Joule heating, etc., with resolution of up to 1 min (Lu et al., 1996, 1998; Ridley et al., 1998). For our study we use AMIE results produced only by 1-min resolution magnetometer data. Using only magnetometers as the AMIE input has certain advantages (Kihn et al., 2006): (a) magnetometers provide a continuous set of observations at a consistent spatial grid with little loss of data, something that radar and satellite measurements cannot do; (b) magnetometers are ubiquitous, offering a nearly global coverage of ionospheric electrodynamics, while the satellite data provide only limited sampling of the ionosphere along the satellite orbit; and (c) no other technique can achieve the same level of continuous global coverage with 1-min resolution. AMIE uses the Fuller-Rowell & Evans (1987) model as the background conductance pattern, and then employs the Ahn et al. (1998) relationship between ground-based magnetometer perturbations and conductances.

According to Faraday's law, the local reconnection rate in the ionosphere, the amount of magnetic flux per unit length along the OCB that becomes open or closed per unit time, is equal to the component of the instantaneous ionospheric electric field at the OCB boundary, parallel to the boundary. This projection yields the convection electric field $\boldsymbol{E}_i$, which is the local reconnection rate due to plasma convection through the OCB boundary. To this we need to add the motional electric field, $\boldsymbol{E}_m = \boldsymbol{v} \times \boldsymbol{B}$, which corresponds to the motion of the boundary with velocity v (perpendicular to the boundary) with B being the Earth's magnetic field, since we need to obtain the plasma motion on the frame of the boundary, $\boldsymbol{E} = \boldsymbol{E}_i + \boldsymbol{v} \times \boldsymbol{B}$ (e.g., Hubert, Milan, et al., 2006). The details of the reconnection rate determination are described in Appendix A.

3.2. February 11, 2000 Pressure Front Reconnection Response

The results for the February 11, 2000 pressure front are shown in Figure 2. The results are obtained every 1 min. Figure 2 shows the calculations at 4 instances, (from top left) one before (2355 UT) and three after (2358, 0010, and 0017 UT) the pressure front impact at 2356 UT. At each time the dial shows the ionospheric potential (black contours) with noon at the top and dawn on the right. The IMF was southward during this period, imposing a typical two-cell potential distribution on the ionosphere. On top of this pattern we plot the OCB obtained from Polar UVI images, and the magnitude of the reconnection electric field (in mV/m), convection plus motional (color coded dots on the OCB). The plot below each dial shows the reconnection electric field as a function of MLT, convection (blue), motional (green), and total (red). The big red diamonds on the dial and the vertical dashed lines on the plot denote the extent of the projection of the dayside reconnection X-line on the ionosphere (see Appendix A for its definition). Between each dial and its associated plot we provide information on the polar cap area in R_E^2, the maximum rate in mV/m, and the total rate or reconnection potential in kV along the dayside (defined by the X-line limits) and the nightside (the remaining OCB).

In the pre-front frame (top left) the dayside and nightside reconnection rates are both below 20 mV/m, with reconnection potentials of about 30 kV. The maximum dayside rate appears near noon, while the maximum nightside rate is located in the post-midnight region. The potential has a two-cell pattern and the X-line projection in the ionosphere spans about 10 h of MLT. The polar cap extends to ∼75° on the dayside and below 70° MLAT on the nightside with area of 0.35 R_E^2. In the first postfront frame (top right), 2 min after the sudden increase in pressure, the potential has been enhanced on the dayside leading to a considerable rise in the dayside reconnection rate that now reaches nearly 65 mV/m and 93.6 kV across a much tighter X-line. The nightside rate has also increased to above 35 mV/m maximum value at post-midnight MLTs, and 64.4 kV overall along the nightside portion of the OCB. The polar cap area is still unchanged at this point. In the next two frames (bottom) the potential continues to intensify, especially on the dawn (positive) side, preserving a significantly enhanced dayside reconnection rate. By now, however, the nightside reconnection rate has significantly increased, with the nightside reconnection potential already overtaking the dayside one. At 0010 UT on February 12, 2000 (bottom left) the nightside rate exhibits three enhancements along the nightside OCB with the maximum rate at 06–07 MLT due to the very distorted nature of the convection pattern. By 0017 UT (bottom right) the maximum has shifted to the 02 MLT region. The polar cap area in the last two frames has started to decrease as the polar cap boundary on the nightside moves poleward, measuring 0.29 R_E^2 at 0010 UT and 0.23 R_E^2 at 0017 UT.

3.3. Reconnection Evolution After the Pressure Front

The reconnection rate calculation of the previous section is fully automated, given the AMIE potential pattern and the Polar UVI polar cap boundary, and as long as a two-cell convection pattern is present which is the case for southward to slightly northward IMF conditions. This allows us to examine the evolution of the dayside/nightside reconnection rates after a dynamic pressure enhancement with 1 min resolution.

Figure 3 illustrates the reconnection evolution with time, on the left based on the AMIE/UVI observations and on the right based on the OpenGGCM simulation. The left plot shows a summary of the reconnection results for the period of 2300 UT on February 11, 2000 to 0100 UT on the next day. The top panel shows the total reconnection electric field (convection plus motional) in mV/m, taken from the 1 min resolution plots of Figure 2, color coded according to the scale on the right. The two white lines cutting along the time axis mark the limits of the dayside reconnection X-line. The middle panel shows the estimated dayside (red) and nightside (blue) total rates (or reconnection potentials) in kV. The bottom panel shows the polar cap area, that is, the area of open flux in the system. The vertical lines at 2356 UT mark the pressure front impact time. For this event, the dayside UVI OCB is only sparsely observed after 0020 UT on 12 February (see Figure 1). In this case, the OCB on the dayside is heavily interpolated in order to produce the reconnection rates, and thus the calculations are unreliable after 0020 UT. This is denoted by the dashed dayside total rate and polar cap area in the bottom two panels.

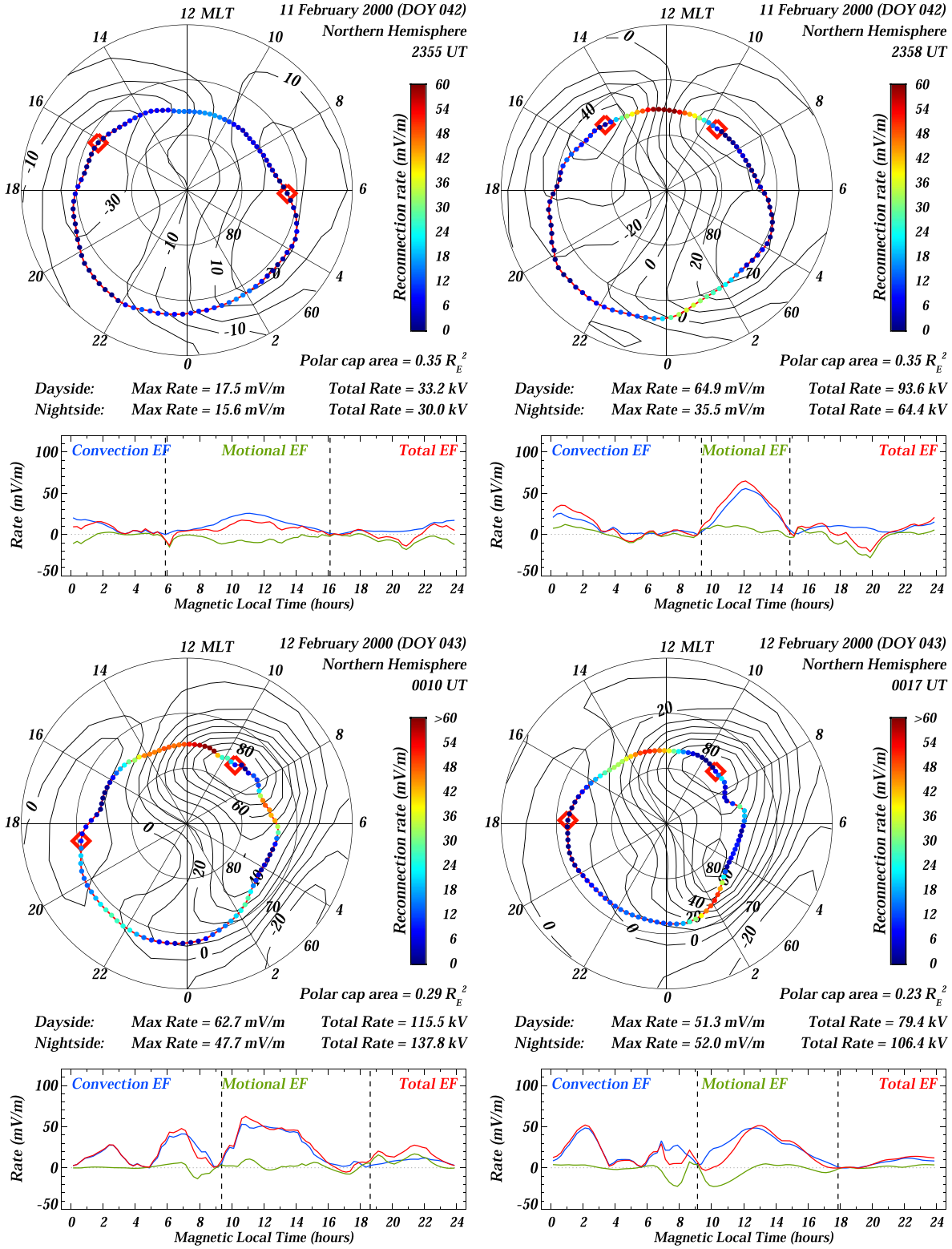

Figure 2. Local reconnection rate calculation using Assimilative Mapping of Ionospheric Electrodynamics (AMIE) and Polar Ultra-Violet Imager (UVI) open-closed field line boundary (OCB) at 4 instances, (from top left) before (2355 UT) and after (2358, 0010, and 0017 UT) the pressure front impact at 2356 UT on February 11, 2000. The dials show the ionospheric potential (black contours), and the reconnection electric field magnitude (color coded dots on the OCB). The plot below each dial shows the reconnection electric field as a function of MLT. The big red diamonds on the dial and the vertical dashed lines on the plot denote the extent of the dayside reconnection X-line.

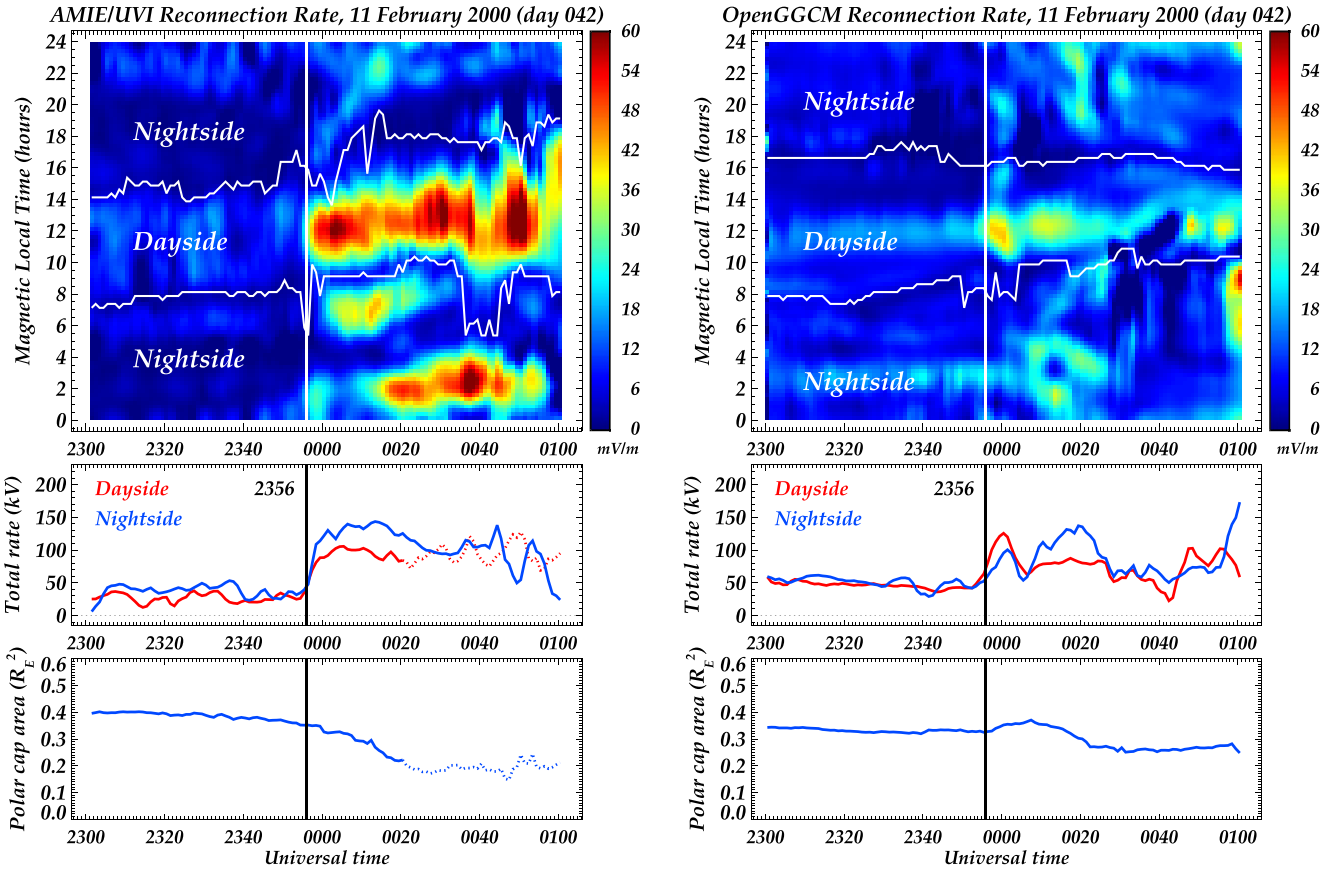

Figure 3. (left) Assimilative Mapping of Ionospheric Electrodynamics (AMIE)/Ultra-Violet Imager (UVI)-determined local reconnection rate (color coded, top panel) as a function of time and MLT for the event of February 11, 2000. The two white lines demarcate the extent of the dayside X-line. The middle panel shows the dayside/nightside reconnection potentials. The bottom panel shows the polar cap area. The vertical lines at 2356 UT mark the pressure front impact time. (right) The same quantities derived using the Open Geospace General Circulation Model (OpenGGCM)-determined polar cap boundary and potential distribution.

The reconnection summary plot shows clearly the response of the dayside and nightside reconnection rates to the incoming pressure front. Before 2356 UT both the dayside and nightside local rates are below 20 mV/m, with the reconnection potentials below 50 kV. At impact there is an immediate and impressive enhancement of the dayside local rate by a factor of about 3–4. This remains unchanged throughout the interval of the plot, even though as mentioned earlier it becomes unreliable after 0020 UT. At the nightside there is an immediate response near midnight by a factor of 2–3 (as was shown in the top right plot of Figure 2). This, however, subsides quickly to be replaced by enhanced reconnection in the 05–08 MLT region that lasts for ~25 min. During the first 10 min on February 12 this is the dominant reconnection region on the nightside. Eventually, after 0015 UT, the post-midnight region becomes the dominant site of the enhanced nightside reconnection, which lasts for about 45 min after.

The reconnection potentials of the middle panel show the strong response of the total rates. Both dayside and nightside potentials rise soon after the front arrival, the nightside exhibiting a stronger response. However, the dayside rate remains steady throughout, while the nightside rate has a peak about 20 min after the front impact and subsides within an hour from impact. Finally, the bottom panel shows quantitatively the previously observed reduction of the magnetospheric open flux after the pressure increase (Figure 1).

The right plot of Figure 3 shows the same quantities as in the left plot, calculated using potential patterns and OCBs produced by the OpenGGCM MHD model. The local reconnection rates of the top panel show a substantial increase after the increase in solar wind pressure, both on the dayside and the nightside. However, the magnitudes and time scales of these changes are different from the observed changes. The dayside rate increases by a factor of 2 in the first 10 min after the pressure front, and gradually decreases during the

next 40 min. The post-midnight rates increase by about 50% 15 min after the pressure increase and last at this level for ~20 min. There is also some increase in the 5–8 MLT sector but much lower than in the data. The pre-midnight rate enhancement is of similar magnitude with the data, but exhibiting different UT-MLT structure.

Even though the model dayside reconnection rates are at a lower level compared with the data ones, the extent of the dayside X-line in the model is greater, leading to slightly higher dayside model rates as seen in the middle panel. In the first 10 min this is also higher than the nightside model potential. The situation, however, reverses in the next 20 min as the postmidnight reconnection rate picks up. The polar cap area of the bottom panel reflects the evolution of the OCB seen in the model plot of Figure 1. It first rises for ~10 min, before it drops to values lower than before the pressure front in another 15 min. This is also in agreement with the reconnection potentials of the middle panel, rising when the dayside rate is higher and dropping once the nightside rate dominates. It is different, however, from the data evolution of the polar cap area, which continuously decreases due to the higher nightside rate after the pressure enhancement.

4. Discussion

4.1. Connection to Previous Studies

The event we presented shows the significant effect solar wind dynamic pressure fronts can have on the polar cap boundary and the dayside/nightside reconnection rates. This response is in agreement with prior results on the effects of dynamic pressure fronts (Boudouridis et al., 2003, 2005, 2007, 2011; Boudouridis, Zesta, Lyons, Anderson, & Lummerzheim, 2004; Boudouridis, Zesta, et al., 2008; Boudouridis, Lyons, et al., 2008; Connor et al., 2014; Hubert et al., 2009). The behavior of the dayside/nightside reconnection potentials was predicted by Boudouridis, Zesta, et al. (2008) who examined the DMSP-measured and AMIE-produced transpolar potential after a pressure front on April 30, 1998. Both datasets showed an initial increase of the potential, which reaches a peak before it fades away leaving a residual value higher than the pre-front potential. Boudouridis, Zesta, et al. (2008) attributed the high post-front peak to enhanced nightside reconnection that soon fades away, and the residual potential to enhanced dayside reconnection under the continued compression of the magnetosphere by the enhanced solar wind dynamic pressure. The present results quantitatively confirm their conclusions.

This interpretation builds on previous results on the responses of the ionospheric convection and the polar cap boundary after sudden P_{SW} enhancements. Boudouridis, Zesta, Lyons, Anderson, & Lummerzheim (2004) studied the differences in the closing of the polar cap after pressure fronts during different concurrent IMF conditions. They concluded that the more extensive closing during southward IMF is due to the compression of a magnetotail loaded with magnetic flux. When the tail is compressed, tail reconnection occurs along the entire width of the tail, producing the nightside and flank polar cap closing and the high nightside reconnection potential. However, when the tail reaches a new equilibrium under the new P_{SW}, the nightside reconnection subsides. On the dayside, Boudouridis et al. (2007) showed that the abrupt increase in dynamic pressure leads to SuperDARN-observed convection enhancements at the apparent location of the cusp. The response is almost immediate, and reaches maximum magnitude within 4 mins of impact. The variation of the dynamic pressure has excellent correlation with the variation of the enhanced convection, leading Boudouridis et al. (2007) to conclude that enhanced dynamic pressure results in a sustained dayside reconnection enhancement.

Boudouridis, Lyons, et al. (2008) used quantitative estimates of the OCB inferred from Polar UVI images (in a method similar to the one used here) and SuperDARN flow measurements to witness ionospheric flow enhancements in the nightside that cross the polar cap boundary following an increase in dynamic pressure, signifying an enhancement in tail reconnection. The onset of the observed reconnection rate response is consistent with the statistical SuperDARN flow response after pressure fronts described by Boudouridis et al. (2011). They showed that the dayside flows react immediately but the nightside flows are delayed by 10–15 min, and attributed this behavior to corresponding enhancements of the dayside and nightside reconnection rates. These same responses are observed in the left panel of Figure 3.

4.2. Potential Tail Reconnection Initiation Mechanisms

Changes in the plasma sheet plasma and magnetic field states in response to IMF B_z direction changes are gradual (of the order of hours) even when the IMF changes are sharp (Terasawa et al., 1997; Wang et al., 2010). In contrast, the plasma sheet plasma pressure is highly correlated with the solar wind dynamic pressure (e.g., Borovsky et al., 1998; Wang et al., 2013). In addition, the changes in plasma pressure and the corresponding magnetic field configurations everywhere in the near-Earth plasma sheet are within a few minutes after the impact of a P_{SW} enhancement on the magnetosphere (Miyashita et al., 2010; Shi et al., 2013; Yue et al., 2013; Zhou et al., 2013). The question that arises now is "what is the physical mechanism for the initiation of the enhanced tail reconnection after a solar wind dynamic pressure front impact?" This question can be addressed in a way similar to the substorm triggering question (e.g., Akasofu, 2017; Mishin et al., 2017; Ebihara, 2019, and references therein). The two main mechanisms discussed in the literature in this context are the Earth-ionosphere waveguide (e.g., Araki, 1977; Kikuchi & Araki, 1979, 2002; Lyons et al., 2013), and the compressional wave propagation through the magnetosphere (e.g., Chi et al., 2001, 2002). In the first mechanism, the pressure front first affects the ionosphere, and then the disturbance propagates into the tail and triggers reconnection. In the second mechanism, the pressure front launches a compressional wave into the magnetosphere, which focuses a large amount of Poynting flux onto the plasma sheet, and triggers reconnection.

The "dripping, tilting bucket" model put forward by Zhou and Tsurutani (2002), outlines the scenarios under which a pressure front facilitates the release of the energy stored in the magnetotail under different preexisting IMF conditions, producing a substorm, pseudo-breakup, or no response at all. According to this model, sustained southward preexisting IMF conditions load the magnetotail with energy. The compression of the magnetotail after a pressure front lowers the threshold for the occurrence of a substorm, further linking the mechanisms responsible for triggering the enhanced tail reconnection during pressure fronts and substorms. This link was further investigated by Lyons et al. (2005), who argued that auroral brightness enhancements after a pressure front impact can be due to a compressive energization of the plasma sheet, a substorm, or both, depending on the interplay of the solar wind pressure enhancement, the preexisting IMF conditions, as well as any concurrent changes in the IMF at the time of impact.

Using multiple Time History of Events and Macroscale Interactions during Substorms (THEMIS) probes to study an interplanetary shock event, Zhou et al. (2013) showed that just a few minutes after the pressure front hit the subsolar magnetopause, the tail current sheet thickness started to decrease, reconnection rate started to increase, and earthward flows started to enhance, signifying a sharp change in the tail structure. They separated the tail effects in two parts. The first response was due to the launch of a compressional wave into the magnetosphere when the shock impinged the subsolar magnetopause. The compressional wave traveled at the magnetosonic speed of 2,900 km/s and reached the tail current sheet within a minute, when the THEMIS spacecraft begun to record changes in the tail structure. The second part of the response was due to the arrival of the external shock compression at the THEMIS X location downtail, which propagated in the solar wind with speed of 550 km/s, and compressed the magnetosphere along the way. This reached the THEMIS probes 3–4 min after the compressional wave.

The nightside reconnection evolution seen near midnight MLT of the left plot of Figure 3 has some of the characteristics described by Zhou et al. (2013). The first reconnection enhancement occurs almost instantaneously, even though of small magnitude (~30 mV/m), and lasts for 5 min. This can be the result of the arrival of the compressional wave, which according to Zhou et al. (2013) causes local magnetic field and plasma fluctuations. The second reconnection enhancement is initiated ~5 min after the end of the first one (~0005 UT), is further enhanced 10 min after that (0015 UT), and reached its peak another 20 min later (0035 UT). The further enhancement at 0015 UT appears to be due to the increased compression of the tail by the arrival of the main pressure front at the downtail location. The peak enhancement at ~0035 UT is perhaps due to an additional peak in the solar wind dynamic pressure, coinciding with further southward turning of the IMF. It is obvious that more events are needed to clearly establish the proper sequence of events in the tail after a solar wind pressure front impact, and determine the reconnection initiation mechanism. Local measurements in the tail, plus modeling of the local tail response will also be greatly beneficial in delineating the physical mechanisms involved.

4.3. Additional Discussion on Caveats

The technique used for the reconnection rate calculation is not specific to the dynamic pressure effects study. It can be used widely for any problem that involves reconnection estimation in magnetospheric physics, as it already has (e.g., Hubert, Milan, et al., 2006, and references therein). There are, however, challenges in the effort to obtain the reconnection rate, as was discussed throughout this article.

It is worth repeating that the most serious challenge is the quality of the OCB determination. In Section 2.1 we discussed the various caveats related to the accuracy of the Polar UVI OCB location determination, and justification for its use. Even though multiple previous studies have demonstrated the ability of polar images in pinpointing this boundary, the boundary resulting from the UVI image processing is not always smooth, or complete for that matter. Even when the imager has full view of the polar ionosphere there are still gaps and irregularities in the boundary determination. An important ensuing issue is the smoothness of the motion of the boundary. This can have a serious effect on the reconnection rate determination, as sudden movements of the boundary from frame to frame (perhaps due to inaccurate identification) will register as strong (but spurious) changes in the reconnection rate, resulting in overestimates of the rate or even strongly negative reconnection rates. To minimize these effects we first remove any point along the determined OCB that is one standard deviation in MLAT away from its neighbors. We then average all the boundaries within 3 min around each AMIE frame (1 min before, 1 min after, and the current minute). Considering that the UVI images have up to 37 s resolution, this interval can include up to four images. The resulting boundary is then interpolated on missing MLT sectors and smoothed in MLT. The poleward or equatorward boundary velocity at each MLT is determined using a 3-point Lagrangian interpolation.

Another issue of the dayside reconnection rate determination is the fact that the cusp aurora appears on open instead of closed field lines, leading to a false identification of the poleward auroral boundary with the OCB. However, Hubert, Milan, et al., 2006 have shown that this introduces only a minimal error in the reconnection rate calculation, in the range of 5%–10% when the convection electric field is strong and 10%–20% when the motional electric field is dominant. One way to mitigate this is to compare the Polar UVI cusp boundary location against publicly available DMSP boundary determinations, which is left for future work.

4.4. Comparison With OpenGGCM Results, Past and Present

As was reported in Sections 2 and 3, the OpenGGCM model has mixed success in reproducing the observations. With the exception of the dayside closing of the polar cap, the model has simulated the salient features of the pressure front response sufficiently well. Both data and model see the nightside and early morning closing of the polar cap. The magnitude of the closing is much higher in the model, as is evident by the different color scales of Figure 1, but the timescales of the response are similar, both within 15–20 min from the front impact. Similarly, the model shows qualitative agreement with the observations when it comes to the reconnection rate response. The simulation records the immediate increase of the dayside reconnection rate, and the pre- and post-midnight enhancements with a delay of 15–20 min. The magnitude of the model response is, however, much more subdued in comparison with the data that witness a tremendous change in the local reconnection rate.

It is worth mentioning here that the model pre-front location of the OCB is reversed compared to the data, exhibiting a lower MLAT location on the dayside and higher MLAT location on the nightside, which is the opposite of what is seen in the UVI measurements. The effect on the post-front response of the model OCB is clear from Figure 1, resulting in much higher nightside post-front values compared to the data, and completely different picture on the dayside. Why this is the state of the pre-front model OCB location, and what effect this might have on the model reconnection rate estimation remains to be investigated with more events in the future.

Connor et al. (2014) used the OpenGGCM-CTIM to study the effects of solar wind dynamic pressure fronts on the transpolar potential and the dayside/nightside reconnection rates. For a pressure step increase event at 0925 UT on April 30, 1998 (that was previously studied by Boudouridis, Zesta, Lyons, Anderson, & Lummerzheim, 2004; Boudouridis, Zesta, et al., 2008), they calculated the model transpolar potential, dayside and nightside reconnection rates. They compared the model transpolar potential to DMSP-derived and AMIE-derived observations. They found significant agreement between the model and the observations.

Both OpenGGCM-CTIM and DMSP track an initial potential increase after the sudden enhancement in dynamic pressure. Despite the fact that the dynamic pressure remains high, both the model and measurements show a subsequent decrease of the transpolar potential. AMIE results qualitatively agree with this response albeit anticipating lower potential magnitude overall. The simulation also estimates the dayside and nightside reconnection rates. It shows that the dayside reconnection rate experiences a dramatic increase within 10 min of the dynamic pressure jump. It then slowly fades away during the next 3 h. The nightside reconnection rate demonstrates a more variable behavior, which includes three consecutive pressure peaks, the first of which manifests ~15 min after the dayside reconnection enhancement.

Our results show qualitative agreement with the Connor et al. (2014) study. More rigorous evaluation of the model response for more events is needed to explore the discrepancies of the data/model reconnection rate and OCB motion, and identify the model parameters that will bridge the gap with the data.

5. Summary and Conclusions

The main conclusion of this study is the direct measurement of the enhanced nightside reconnection rate after the impact of a solar wind dynamic pressure front. This nightside reconnection enhancement was only postulated in the past, based on the closing of the polar cap and enhancement of ionospheric convection, but was never directly measured. For the first time, we performed this calculation using the combined Polar UVI/AMIE datasets, and proved that a significant increase in tail reconnection occurs in connection with the impact of a solar wind pressure front. The tail reconnection enhancement, as seen in the nightside reconnection potential (left middle panel of Figure 3), peaks in about 20 min after the pressure front impact, after which time it slowly subsides. We suggest that the 20 min timescale is the time it takes for the magnetotail to reconfigure itself after the sudden compression from the increased P_{SW} regime. The tail is now balanced at a new external compression level, thus not supporting further reconnection rate enhancements.

A more detailed account of the conclusions reached with respect to the UVI/AMIE observations of this study is as follows:

1. The polar cap size is reduced after a pressure front impact. The reduction is more evident on the nightside but also present on the dayside.
2. The response of the OCB motion is nearly immediate on the dayside and early morning MLT sectors, reaching maximum displacement in 10–20 min. The midnight region's response is initiated ~10 min from impact, and reach maximum effect in another ~10 min.
3. In terms of the reconnection rate, the data demonstrate a strong response on both the dayside and the nightside magnetosphere, with rates rising considerably from pre-front values. The nightside effects are most significant first in the 5–8 MLT sector and then in the postmidnight MLT sector. The details of the MLT distribution of the nightside reconnection rate might be dependent on the specific event characteristics (solar wind properties, polar region potentials, and polar cap boundary), but the total nightside reconnection rate exhibits a clear pressure-front related enhancement.
4. As with the OCB, the dayside response is immediate after the arrival of the pressure front. The 5–8 MLT sector reacts 5 min after impact, while the main postmidnight response is first witnessed within ~20 min after the pressure jump.

The above conclusions stem from this particular study. The closing of the polar cap has been observed in other events, but the MLT/time delay details might differ from case to case. The reconnection rate changes recorded in this case are novel observations, but we strongly believe the most salient features are applicable to other pressure front events under southward IMF conditions.

The study also utilized the OpenGGCM global MHD model for comparison with the UVI/AMIE observations. The comparison has revealed several agreements and disagreements with the data. The following are its key points:

1. The OpenGGCM model simulations of the OCB agree qualitatively with the data on the nightside and morning MLT sectors. The timescales of the model response are similar to the data in these sectors. The magnitude of the model response is, however, much stronger.

Table 1
Summary of the Open-Closed Boundary Results

MLT Range (hours)	Open-Closed Boundary			
	Observations		OpenGGCM	
	MLAT	Time delay	MLAT	Time delay
00-01	66°–68° to 74°–76°	15 min	74°–80° to >84°	20 min
01-02				
02-03	66° to 80°	4 min to 74° 20 min to 80°		
03-04				
04-05				
05-06				
06-07	74°–76° to >78°	10 min to 77° 20 min to >78°	68°–70° to 76°–84°	20 min
07-08				
08-09				
09-10				
10-11	75° to 76°	2 min	66°–68° to 70°–74°	40 min
11-12				
12-13			66°–68° to 64°–66°	2–4 min
13-14				
14-15	No reliable data	No reliable data		
15-16				
16-17			68°–70° to 66°–68°	4–8 min
17-18				
18-19			72°–74° to >82°	20 min
19-20				
20-21	66°–68° to 74°–76°	15 min		
21-22				
22-23				
23-24				

2. The model noon-to-afternoon response is opposite of that of the data, showing a slight opening of the polar cap in these MLT sectors, at least during the first hour after impact.
3. The pre-front model assessment of the OCB is reversed in comparison with the data, showing that the OCB's initial location was at low MLAT at dayside and high MLAT at nightside.
4. The OpenGGCM model reconnection rates increase with timescales similar to the observations, but exhibit much reduced post-front magnitude, and shorter duration for the ensuing enhanced reconnection.

We should mention that the comparison with the model was meant to showcase that the particular model with its current setup cannot entirely simulate the pressure front response in terms of the polar cap boundary motion and reconnection rates estimate. The purpose of the side-by-side comparison was not to

Table 2
Summary of the Reconnection Rate Results

MLT Range (hours)	Reconnection Rate			
	Observations		OpenGGCM	
	Magnitude	Time delay	Magnitude	Time delay
00-01	<10 mV/m to 25 mV/m then to >40 mV/m	2 min initially 20 min main response	<20 mV/m to 25–35 mV/m	12 min
01-02				
02-03				
03-04				
04-05	No response	No response		
05-06	10 mV/m to 20–40 mV/m	5 min	No significant response	No significant response
06-07				
07-08				
08-09	No significant response	No significant response		
09-10				
10-11	10–20 mV/m to >50 mV/m	2 min	20 mV/m to 30–40 mV/m	2 min
11-12				
12-13				
13-14				
14-15	No significant response	No significant response	No significant response	No significant response
15-16				
16-17				
17-18				
18-19			<10 mV/m to 20–30 mV/m	2–4 min initially at 18–21 MLT 20 min main response
19-20				
20-21				
21-22	10–15 mV/m to 25 mV/m	20 min		
22-23				
23-24				

determine the faults of the model that lead to its inaccurate assessment of this case, but to provide a starting point for future work by the modelers in an effort to improve the model, so that sharp changes in solar wind dynamic pressure can be more correctly incorporated in the model simulation of the magnetosphere. Even though the OpenGGCM-CTIM can realistically describe the ionospheric electrodynamics during space weather events (as mentioned in Section 2.2), it still cannot accurately account for the OCB and reconnection rate changes during pressure front events.

The results of the study in terms of both magnitude of the response and response time, observations and modeling, are comprehensively outlined in Tables 1 and 2, for the OCB and reconnection rates, respectively.

This is a rough depiction of the understanding of Figures 1 and 3, which should be consulted for a more detailed picture of the responses.

Finally, the reconnection rate calculation used in this study is fully automated, given the AMIE potential pattern and the Polar UVI polar cap boundary location. The only other limitation is that the accurate dayside reconnection X-line length determination requires a potential distribution that resembles a two-cell convection pattern. This requirement is necessary for the estimation of the dayside/nightside reconnection potentials. Therefore, the described technique works for southward or slightly northward IMF conditions. We should emphasize again that the described technique can be used widely for any problem that involves reconnection estimation in magnetospheric physics, beyond the narrow scope of the present study of the effects of solar wind dynamic pressure fronts.

Appendix A: Reconnection Rate Calculations

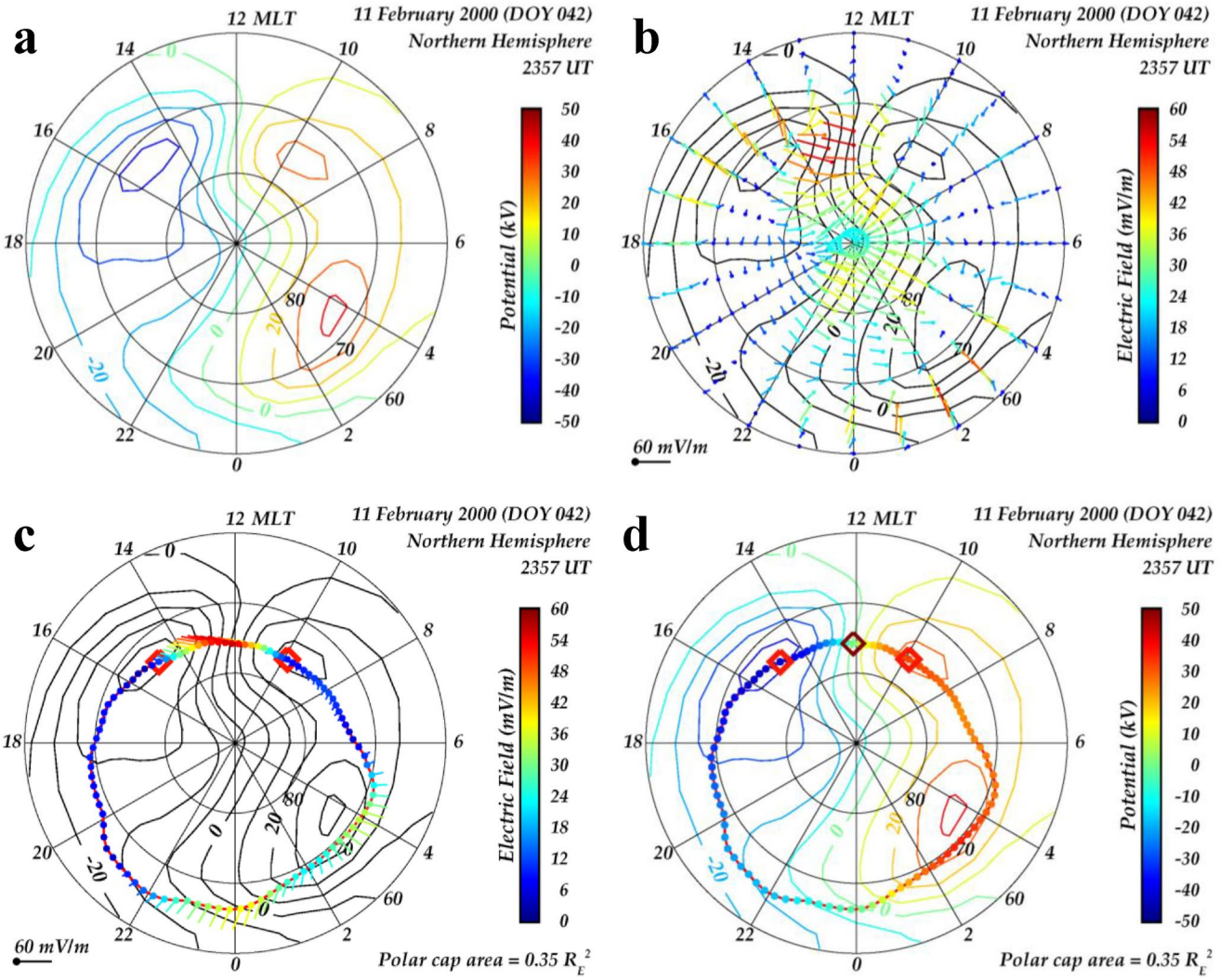

Figure A1. Steps in the determination of the reconnection rate from ionospheric measurements (example for 2357 UT on February 11, 2000): (a) Assimilative Mapping of Ionospheric Electrodynamics (AMIE) ionospheric potential distribution, (b) 2-dimensional ionospheric electric field, (c) ionospheric electric field vectors interpolated on the OCB location, and (d) determination of the extent of the X-line based on the potential distribution and the Ultra-Violet Imager (UVI) open-closed field line boundary (OCB) location.

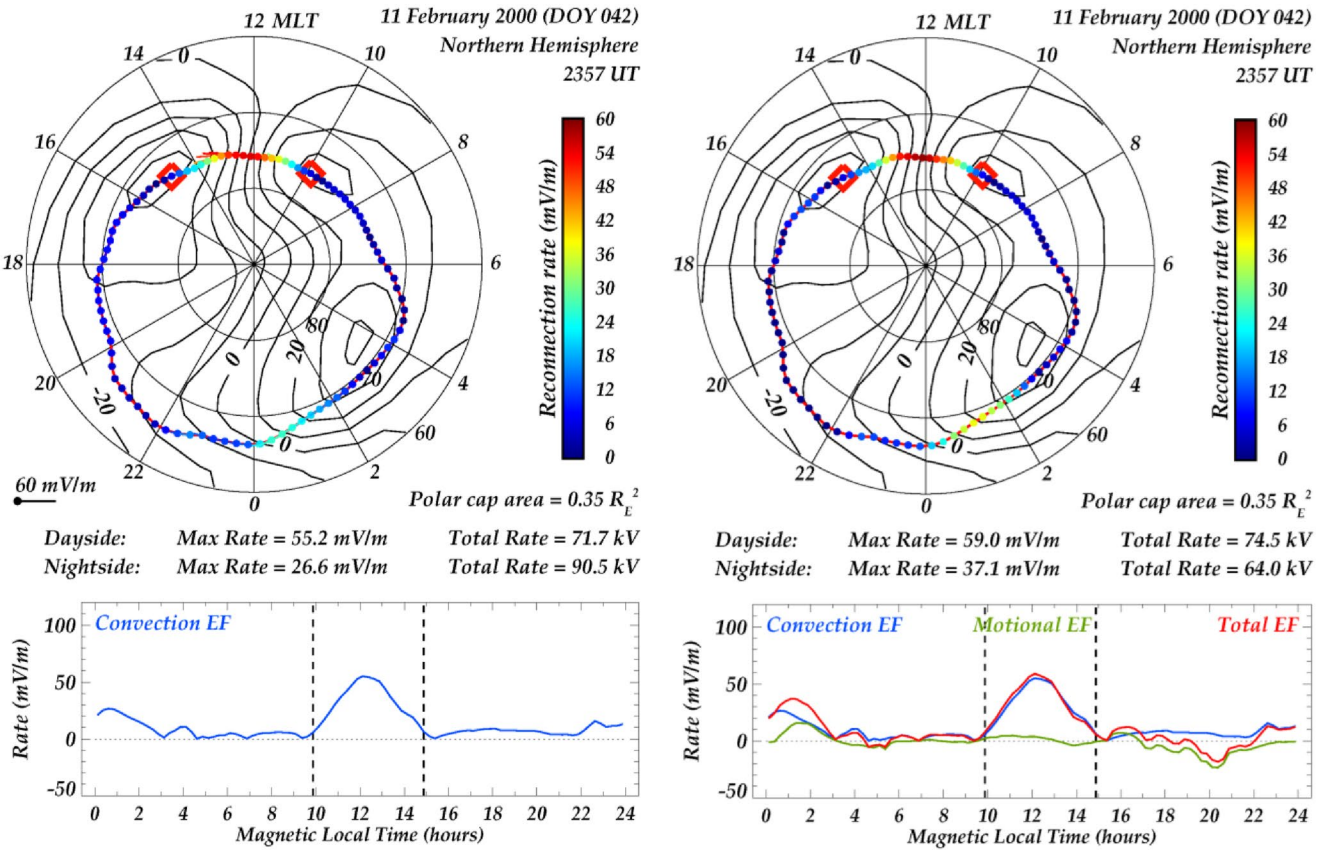

Figure A2. Final steps in the reconnection rate calculation for 2357 UT on February 11, 2000. (left) The open-closed field line boundary (OCB) electric field component parallel to the boundary is the convection electric field, shown in the panel below the dial. (right) The total electric field, convection plus motional (red in the panel below the dial), yields the reconnection rate along the OCB. The format of the two plots is the same as in Figure 2.

We begin with the potential distribution in the ionosphere deduced by AMIE. The AMIE potentials are provided at 24 MLT sectors and every 2° MLAT from the pole to 44°. Figure A1 panel (a) shows the potential distribution at 2357 UT on February 11, 2000, as contours color-coded with the scale on the right of the dial. Noon is at the top and dusk on the left for all four panels of Figure A1, with MLAT circles limited between 60° and 90°. In this color scheme the zero potential curve is green and separates the positive potentials (yellow to red) from the negative potentials (cyan to blue).

The electric field distribution over the same region is obtained by differentiating the potential in two directions, eastward and poleward, since $E = -\nabla\Phi$. Figure A1 panel (b) shows the total vector ionospheric electric field distribution on the same regular grid as the potential distribution of panel (a). The location of each electric field vector is marked by a dot, with its direction indicated by a line, the length of which is proportional to the magnitude of the total field (according to the arrow at the bottom left of the dial), and color-coded with the scale on the right.

The two electric field components are then estimated for the OCB MLT/MLAT location determinations by interpolating the given regular grid values, thus providing the total electric field vector on the boundary location. Figure A1 panel (c) shows the interpolated total electric field vectors on the OCB boundary, which was determined with the technique described in Section 2. The arrow length and color of the field follow the conventions established for panel (b).

Finally, Figure A1 panel (d) illustrates the technique for determining the length of the projection of the dayside X-line on the ionosphere. The dayside X-line is the line along the dayside magnetosphere where field line reconnection occurs. The calculation of the dayside/nightside reconnection potentials of Figures 2

and 3 depend on the accurate determination of the dayside X-line extent. In panel (d) we plot again the AMIE potentials in the same format as in panel (a), and overplot the UVI OCB color-coded with the local potential value. The projection of the dayside X-line is defined as the boundary portion through which the ionospheric plasma flows anti-sunward (into the polar cap). This definition assumes southward IMF conditions and a two-cell convection pattern.

We proceed by first identifying the point on the dayside OCB where the zero potential contour intersects the boundary (big brown diamond). We then move on both dawnward and duskward directions looking for the points where the potential slope changes sign for the first time. At the dawn side this will be from positive to negative, and the opposite for the dusk side (big red diamonds). The portion of the dayside boundary between these two points is the dayside reconnection X-line projection on the ionosphere. There are some technical issues with this identification. First, when the IMF is strongly in the dawn-dusk direction, the two-cell pattern is so distorted that the accurate identification of the zero potential curve on the dayside with automated techniques becomes problematic. Another issue arises when the boundary is at low latitudes (or the two-cell pattern is at higher latitudes). In this case, following the boundary on either dusk or dawn (or both) can proceed parallel to the equipotential lines, leading to an unrealistically long dayside X-line, occasionally reaching deep into the nightside.

The final steps in the reconnection rate calculation for 2357 UT on February 11, 2000 are illustrated in Figure A2. The component of the OCB vector electric field of panel (c) in the direction parallel to the boundary in each 15 min MLT sector yields the convection electric field $\boldsymbol{E_i}$. This represents the reconnection rate due to plasma convection through the boundary. The left plot of Figure A2 shows the convection electric field vectors parallel to the OCB (visible only on the dayside at this magnitude), color-coded with the scale on the right, and plotted as function of MLT at the panel below the dial.

An additional component of the reconnection rate is due to the motional electric field, $\boldsymbol{E_m} = \boldsymbol{v} \times \boldsymbol{B}$, which corresponds to the motion of the boundary with velocity v (perpendicular to the boundary), where B is the Earth's magnetic field. This is necessary to obtain the plasma motion on the frame of the boundary, $\boldsymbol{E} = \boldsymbol{E_i} + \boldsymbol{v} \times \boldsymbol{B}$ (Siscoe & Huang, 1985; Hubert, Milan, et al., 2006). The total reconnection rate is shown in the right plot of Figure A2, color-coded in the same manner, and plotted in red as a function of MLT in the panel below the dial.

Data Availability Statement

The authors wish to thank James Weygand of the University of California at Los Angeles for the propagated solar wind and IMF data which can be found at http://vmo.igpp.ucla.edu/data1/Weygand/. The polar UVI data can be found at the CDAWeb website https://cdaweb.gsfc.nasa.gov/index.html/. The AMIE results can be found at http://vmr.engin.umich.edu/Model/_amie/plot.php. The OpenGGCM model can be run at the Community Coordinated Modeling Center website https://ccmc.gsfc.nasa.gov/index.php.

Acknowledgments
The authors are grateful to Chih-Ping Wang of the University of California at Los Angeles, and Joachim Raeder of the University of New Hampshire for useful discussions. The work by Athanasios Boudouridis at the Space Science Institute (SSI) was supported by NASA Geospace Sciences award NNX-11AJ07G. Hyunju K. Connor gratefully acknowledges support from NSF grants OIA-1920965 and AGS-1928883, and NASA grants 80NSSC19K0844, 80NSS-C18K104, and 80NSSC18K1052.

References

Ahn, B.-H., Richmond, A. D., Kamide, Y., Kroehl, H. W., Emery, B. A., de la Beaujardiére, O., & Akasofu, S.-I. (1998). An ionospheric conductance model based on ground magnetic disturbance data. *Journal of Geophysical Research*, *103*, 14769–14780. https://doi.org/10.1029/97ja03088

Akasofu, S.-I. (1980). The solar wind-magnetosphere energy coupling and magnetospheric disturbances. *Planetary and Space Science*, *28*, 495–509. https://doi.org/10.1016/0032-0633(80)90031-8

Akasofu, S.-I. (2017). Auroral substorms: Search for processes causing the expansion phase in terms of the electric current approach. *Space Science Reviews*, *212*, 341–381. https://doi.org/10.1007/s11214-017-0363-7

Araki, T. (1977). Global structure of geomagnetic sudden commencements. *Planetary and Space Science*, *25*, 373–384. https://doi.org/10.1016/0032-0633(77)90053-8

Baker, J. B., Clauer, C. R., Ridley, A. J., Papitashvili, V. O., Brittnacher, M. J., & Newell, P. T. (2000). The nightside poleward boundary of the auroral oval as seen by DMSP and the ultraviolet imager. *Journal of Geophysical Research*, *105*(A9), 21267–21280. https://doi.org/10.1029/1999ja000363

Borovsky, J. E., Thomsen, M. F., & Elphic, R. C. (1998). The driving of the plasma sheet by the solar wind. *Journal of Geophysical Research*, *103*, 17617–17640. https://doi.org/10.1029/97ja02986

Boudouridis, A., Lyons, L. R., Zesta, E., & Ruohoniemi, J. M. (2007). Dayside reconnection enhancement resulting from a solar wind dynamic pressure increase. *Journal of Geophysical Research*, *112*, A06201. https://doi.org/10.1029/2006JA012141

Boudouridis, A., Lyons, L. R., Zesta, E., Ruohoniemi, J. M., & Lummerzheim, D. (2008). Nightside flow enhancement associated with solar wind dynamic pressure driven reconnection. *Journal of Geophysical Research*, *113*, A12211. https://doi.org/10.1029/2008JA013489

Boudouridis, A., Lyons, L. R., Zesta, E., Weygand, J. M., Ribeiro, A. J., & Ruohoniemi, J. M. (2011). Statistical study of the effect of solar wind dynamic pressure fronts on the dayside and nightside ionospheric convection. *Journal of Geophysical Research*, *116*, A10233. https://doi.org/10.1029/2011JA016582

Boudouridis, A., Zesta, E., Lyons, L. R., & Anderson, P. C. (2004). Evaluation of the hill-siscoe transpolar potential saturation model during a solar wind dynamic pressure pulse. *Geophysical Research Letters*, *31*, L23802. https://doi.org/10.1029/2004GL021252

Boudouridis, A., Zesta, E., Lyons, L. R., Anderson, P. C., & Lummerzheim, D. (2003). Effect of solar wind pressure pulses on the size and strength of the auroral oval. *Journal of Geophysical Research*, *108*(A4), 8012. https://doi.org/10.1029/2002JA009373

Boudouridis, A., Zesta, E., Lyons, L. R., Anderson, P. C., & Lummerzheim, D. (2004). Magnetospheric reconnection driven by solar wind pressure fronts. *Annales Geophysicae*, *22*, 1367–1378. https://doi.org/10.5194/angeo-22-1367-2004

Boudouridis, A., Zesta, E., Lyons, L. R., Anderson, P. C., & Lummerzheim, D. (2005). Enhanced solar wind geoeffectiveness after a sudden increase in dynamic pressure during southward IMF orientation. *Journal of Geophysical Research*, *110*, A05214. https://doi.org/10.1029/2004JA010704

Boudouridis, A., Zesta, E., Lyons, L. R., Anderson, P. C., & Ridley, A. J. (2008). Temporal evolution of the transpolar potential after a sharp enhancement in solar wind dynamic pressure. *Geophysical Research Letters*, *35*, L02101. https://doi.org/10.1029/2007GL031766

Boyle, C. B., Reiff, P. H., & Hairston, M. R. (1997). Empirical polar cap potentials. *Journal of Geophysical Research*, *102*(A1), 111–125. https://doi.org/10.1029/96JA01742

Brittnacher, M., Fillingim, M., Parks, G., Germany, G., & Spann, J. (1999). Polar cap area and boundary motion during substorms. *Journal of Geophysical Research*, *104*(A6), 12251–12262. https://doi.org/10.1029/1998JA900097

Carbary, J. F., Sotirelis, T., Newell, P. T., & Meng, C.-I. (2003). Auroral boundary correlations between UVI and DMSP. *Journal of Geophysical Research*, *108*(A1), 1018. https://doi.org/10.1029/2002JA009378

Chi, P. J., Russell, C. T., Raeder, J., Zesta, E., Yumoto, K., Kawano, H., et al. (2001). Propagation of the preliminary reverse impulse of sudden commencements to low latitudes. *Journal of Geophysical Research*, *106*, 18857–18864. https://doi.org/10.1029/2001ja900071

Chi, P. J., Russell, C. T., Raeder, J., Zesta, E., Yumoto, K., Kawano, H., et al. (2002). Reply to comment by T. Kikuchi and T. Araki on "Propagation of the preliminary reverse impulse of sudden commencements to low latitudes". *Journal of Geophysical Research*, *107*(A12), 1474. https://doi.org/10.1029/2002JA009369

Chua, D., Parks, G., Brittnacher, M., Germany, G., Spann, J., Spann, J., & Carlson, C. (2001). Energy characteristics of auroral electron precipitation: A comparison of substorms and pressure pulse related auroral activity. *Journal of Geophysical Research*, *106*, 5945–5956. https://doi.org/10.1029/2000ja003027

Codrescu, M. V., Negrea, C., Fedrizzi, M., Fuller-Rowell, T. J., Dobin, A., Jakowsky, N., et al. (2012). A real-time run of the coupled thermosphere ionosphere plasmasphere electrodynamics (CTIPe) model. *Space Weather*, *10*, S02001. https://doi.org/10.1029/2011SW000736

Connor, H. K., Zesta, E., Fedrizzi, M., Shi, Y., Raeder, J., Codrescu, M. V., & Fuller-Rowell, T. J. (2016). Modeling the ionosphere-thermosphere response to a geomagnetic storm using physics-based magnetospheric energy input: Open GGCM-CTIM results. *Journal of Space Weather and Space Climate*, *6*, A25. https://doi.org/10.1051/swsc/2016019

Connor, H. K., Zesta, E., Ober, D. M., & Raeder, J. (2014). The relation between transpolar potential and reconnection rates during sudden enhancement of solar wind dynamic pressure: Open GGCM-CTIM results. *Journal of Geophysical Research: Space Physics*, *119*, 3411–3429. https://doi.org/10.1002/2013JA019728

Cowley, S. W. H. (1984). Solar wind control of magnetospheric convection. In B. Battrick, & E. Rolfe (Eds.), *Achievements of the international magnetospheric study (IMS)* (p. 483–494). Netherlands: European Space Agency.

Ebihara, Y. (2019). Simulation study of near-earth space disturbances: 2. Auroral substorms. *Progress in Earth and Planetary Science*, *6*, 24. https://doi.org/10.1186/s40645-019-0273-2

Fuller-Rowell, T., & Evans, D. (1987). Height-integrated pedersen and hall conductivity patterns inferred from TIROS–NOAA satellite data. *Journal of Geophysical Research*, *92*, 7606–7618. https://doi.org/10.1029/JA092iA07p07606

Fuller-Rowell, T. J., Rees, D., Quegan, S., Moffett, R. J., Codrescu, M. V., Millward, G. H., & Schunk, R. W. (1996). *A coupled thermosphere-ionosphere model (CTIM)* (pp. 217). Colorado: STEP Report.

Fuselier, S. A., & Lewis, W. S. (2011). Properties of near-earth magnetic reconnection from in-situ observations. *Space Science Reviews*, *160*, 95–121. https://doi.org/10.1007/s11214-011-9820-x

Holmes, J. M., Johnsen, M. G., Deehr, C. S., Zhou, X.-Y., & Lorentzen, D. A. (2014). Circumpolar ground-based optical measurements of proton and electron shock aurora. *Journal of Geophysical Research: Space Physics*, *119*, 3895–3914. https://doi.org/10.1002/2013JA019574

Hubert, B., Blockx, C., Milan, S. E., & Cowley, S. W. H. (2009). Statistical properties of flux closure induced by solar wind dynamic pressure fronts. *Journal of Geophysical Research*, *114*, A07211. https://doi.org/10.1029/2008JA013813

Hubert, B., Milan, S. E., Grocott, A., Cowley, S. W. H., Gérard, J.-C., & Gérard, J.-C. (2006). Dayside and nightside reconnection rates inferred from IMAGE-FUV and SuperDARN data. *Journal of Geophysical Research*, *111*, A03217. https://doi.org/10.1029/2005JA011140

Hubert, B., Palmroth, M., Laitinen, T. V., Janhunen, P., Milan, S. E., Grocott, A., et al. (2006). Compression of the earth's magnetotail by interplanetary shocks directly drives transient magnetic flux closure. *Geophysical Research Letters*, *33*, L10105. https://doi.org/10.1029/2006GL026008

Kauristie, K., Weygand, J., Pulkkinen, T. I., Murphree, J. S., & Newell, P. T. (1999). Size of the auroral oval: UV ovals and precipitation boundaries compared. *Journal of Geophysical Research*, *104*(A2), 2321–2331. https://doi.org/10.1029/1998ja900046

Kelley, M. C. (1989). *The Earth's ionosphere*. NewYork: Academic Press.

Kennel, C. F., & Petschek, H. E. (1966). Limit on stably trapped particle fluxes. *Journal of Geophysical Research*, *71*, 1–28. https://doi.org/10.1029/jz071i001p00001

Kihn, E. A., Redmon, R., Ridley, A. J., & Hairston, M. R. (2006). A statistical comparison of the AMIE derived and DMSP-SSIES observed high-latitude ionospheric electric field. *Journal of Geophysical Research*, *111*, A08303. https://doi.org/10.1029/2005JA011310

Kikuchi, T., & Araki, T. (1979). Horizontal transmission of the polar electric field to the equator. *Journal of Atmospheric and Terrestrial Physics*, *41*, 927–936. https://doi.org/10.1016/0021-9169(79)90094-1

Kikuchi, T., & Araki, T. (2002). Comment on "Propagation of the preliminary reverse impulse of sudden commencements to low latitudes" by P. J. Chi et al. *Journal of Geophysical Research*, *107*(A12), 1473. https://doi.org/10.1029/2001JA009220

Knight, S. (1973). Parallel electric fields. *Planetary and Space Science*, *21*, 741–750. https://doi.org/10.1016/0032-0633(73)90093-7

Liou, K. (2006). Global auroral response to interplanetary media with emphasis on solar wind dynamic pressure enhancements. In B. Tsurutani, et al. (Eds.), *Recurrent magnetic storms: Corotating solar wind streams, geophys. Monogr. Ser.* (Vol. 167, pp. 197–212). Washington, D.C: American Geophysical Union. https://doi.org/10.1029/167gm17

Lu, G., Baker, D. N., McPherron, R. L., Farrugia, C. J., Lummerzheim, D., Ruohoniemi, J. M., et al. (1998). Global energy deposition during the January 1997 magnetic cloud event. *Journal of Geophysical Research*, *103*(A6), 11685–11694. https://doi.org/10.1029/98JA00897

Lu, G., Emery, B. A., Rodger, A. S., Lester, M., Taylor, J. R., Evans, D. S., et al. (1996). High-latitude ionospheric electrodynamics as determined by the assimilative mapping of ionospheric electrodynamics procedure for the conjunctive SUNDIAL/ATLAS 1/GEM period of March 28–29. 1992. *Journal of Geophysical Research*, *101*(A12), 26697–26718. https://doi.org/10.1029/96JA00513

Lummerzheim, D., Brittnacher, M., Evans, D., Germany, G. A., Parks, G. K., Rees, M. H., & Spann, J. F. (1997). High time resolution study of the hemispheric power carried by energetic electrons into the ionosphere during the May 19/20, 1996 auroral activity. *Geophysical Research Letters*, *24*, 987–990. https://doi.org/10.1029/96gl03828

Lyons, L. R. (2000). Geomagnetic disturbances: Characteristics of, distinction between types, and relations to interplanetary conditions. *Journal of Atmospheric and Solar-Terrestrial Physics*, *62*, 1087–1114. https://doi.org/10.1016/s1364-6826(00)00097-3

Lyons, L. R., Evans, D., & Lundin, R. (1979). An observed relation between magnetic field aligned electric fields and downward electron energy fluxes in the vicinity of auroral forms. *Journal of Geophysical Research*, *84*, 457–461. https://doi.org/10.1029/ja084ia02p00457

Lyons, L. R., Lee, D.-Y., Wang, C.-P., & Mende, S. B. (2005). Global auroral responses to abrupt solar wind changes: Dynamic pressure, substorm, and null events. *Journal of Geophysical Research*, *110*, A08208. https://doi.org/10.1029/2005JA011089

Lyons, L. R., Nishimura, Y., Donovan, E., & Angelopoulos, V. (2013). Distinction between auroral substorm onset and traditional ground magnetic onset signatures. *Journal of Geophysical Research: Space Physics*, *118*, 4080–4092. https://doi.org/10.1002/jgra.50384

Milan, S. E., Cowley, S. W. H., Lester, M., Wright, D. M., Slavin, J. A., Fillingim, M., et al. (2004). Response of the magnetotail to changes in the open flux content of the magnetosphere. *Journal of Geophysical Research*, *109*, A04220. https://doi.org/10.1029/2003JA010350

Mishin, V. M., Mishin, V. V., Lunyushkin, S. B., Wang, J. Y., & Moiseev, A. V. (2017). 27 August 2001 substorm: Preonset phenomena, two main onsets, field-aligned current systems, and plasma flow channels in the ionosphere and in the magnetosphere. *Journal of Geophysical Research: Space Physics*, *122*, 4988–5007. https://doi.org/10.1002/2017JA023915

Miyashita, Y., Keika, K., Liou, K., Machida, S., Kamide, Y., Miyoshi, Y., et al. (2010). Plasma sheet changes caused by sudden enhancements of the solar wind pressure. *Journal of Geophysical Research*, *115*, A05214. https://doi.org/10.1029/2009JA014617

Newell, P. T., Feldstein, Y. I., Galperin, Y. I., & Meng, C.-I. (1996). Morphology of nightside precipitation. *Journal of Geophysical Research*, *101*(A5), 10737–10748. https://doi.org/10.1029/95ja03516

Oliveira, D. M., & Raeder, J. (2014). Impact angle control of interplanetary shock geoeffectiveness. *Journal of Geophysical Research: Space Physics*, *119*, 8188–8201. https://doi.org/10.1002/2014JA020275

Oliveira, D. M., & Raeder, J. (2015). Impact angle control of interplanetary shock geoeffectiveness: A statistical study. *Journal of Geophysical Research: Space Physics*, *120*, 4313–4323. https://doi.org/10.1002/2015JA021147

Ozturk, D. S., Zou, S., Ridley, A. J., & Slavin, J. A. (2018). Modeling study of the geospace system response to the solar wind dynamic pressure enhancement on 17 March 2015. *Journal of Geophysical Research: Space Physics*, *123*, 2974–2989. https://doi.org/10.1002/2017JA025099

Paschmann, G., Øieroset, M., & Phan, T. (2013). In-situ observations of reconnection in space. *Space Science Reviews*, *178*, 385–417. https://doi.org/10.1007/s11214-012-9957-2

Pulkkinen, A., Rastätter, L., Kuznetsova, M., Singer, H., Balch, C., Weimer, D., et al. (2013). Community-wide validation of geospace model ground magnetic field perturbation predictions to support model transition to operations. *Space Weather*, *11*, 369–385. https://doi.org/10.1002/swe.20056

Raeder, J. (2003). Global magnetohydrodynamics – A Tutorial. In J. Buechner, C. T. Dum, & M. Scholer (Eds.), *Space plasma simulation, lecture notes in physics* (Vol. 615). Heidelberg: Springer Verlag.

Raeder, J. (2006). Flux transfer events: 1. Generation mechanism for strong southward IMF. *Annales Geophysicae*, *24*, 381–392. https://doi.org/10.5194/angeo-24-381-2006

Raeder, J., Larson, D., Li, W., Kepko, E. L., & Fuller-Rowell, T. (2008). Open GGCM simulations for the THEMIS mission. *Space Science Reviews*, *141*, 535–555. https://doi.org/10.1007/s11214-008-9421-5

Raeder, J., McPherron, R. L., Frank, L. A., Kokubun, S., Lu, G., Mukai, T., et al. (2001). Global simulation of the geospace environment modeling substorm challenge event. *Journal of Geophysical Research*, *106*(A1), 381–395. https://doi.org/10.1029/2000ja000605

Raeder, J., Wang, Y. L., & Fuller-Rowell, T. J. (2001). Geomagnetic storm simulation with a coupled magnetosphere-ionosphere-thermosphere model. In P. Song, H. J. Singer, & G. Siscoe (Eds.), *Space weather: Progress and challenges in Research and applications, geophys. Monogr. Ser* (Vol. 125, pp. 377–384). Washington,D.C: American Geophysical Union.

Rich, F. J., & Hairston, M. R. (1994). Large-scale convection patterns observed by DMSP. *Journal of Geophysical Research*, *99*(A3), 3827–3844. https://doi.org/10.1029/93JA03296

Richmond, A. D., & Kamide, Y. (1988). Mapping electrodynamic features of the high-latitude ionosphere from localized observations: Technique. *Journal of Geophysical Research*, *93*, 5741–5759. https://doi.org/10.1029/ja093ia06p05741

Ridley, A. J., Lu, G., Clauer, C. R., & Papitashvili, V. O. (1998). A statistical study of the ionospheric convection response to changing interplanetary magnetic field conditions using the assimilative mapping of ionospheric electrodynamics technique. *Journal of Geophysical Research*, *103*, 4023–4039. https://doi.org/10.1029/97ja03328

Robinson, R. M., Vondrak, R. R., Miller, K., Dabbs, T., & Hardy, D. (1987). On calculating ionospheric conductances from the flux and energy of precipitating electrons. *Journal of Geophysical Research*, *92*, 2565–2569. https://doi.org/10.1029/ja092ia03p02565

Shi, Q.-Q., Hartinger, M., Angelopoulos, V., Zong, Q.-G., Zhou, X.-Z., Zhou, X.-Y., et al. (2013). THEMIS observations of ULF wave excitation in the nightside plasma sheet during sudden impulse events. *Journal of Geophysical Research: Space Physics*, *118*, 284–298. https://doi.org/10.1029/2012JA017984

Siscoe,G.L.,&Huang,T.S.(1985).Polarcapinflationanddeflation.*JournalofGeophysicalResearch*,*90*,543–547.https://doi.org/10.1029/ja090ia01p00543

Terasawa, T., Fujimoto, M., Mukai, T., Shinohara, I., Saito, Y., Yamamoto, T., et al. (1997). Solar wind control of density and temperature in the near-Earth plasma sheet: WIND/GEOTAIL collaboration. *Geophysical Research Letters*, *24*, 935–938. https://doi.org/10.1029/96GL04018

Vasyliunas, V. M. (1970). Mathematical models of magnetospheric convection and its coupling to the ionosphere. In B. M. McCormac, & D. Reidel (Eds.), *Particles and fields in the magnetosphere* (Vol. 17, pp. 60–71). Springer. https://doi.org/10.1007/978-94-010-3284-1_6

Wang, C. -P., Lyons, L. R., Nagai, T., Weygand, J. M., & Lui, A. T. Y. (2010). Evolution of plasma sheet particle content under different interplanetary magnetic field conditions. *Journal of Geophysical Research*, *115*, A06210. https://doi.org/10.1029/2009JA015028

Wang, C.-P., Yue, C., Zaharia, S., Xing, X., Lyons, L., Angelopoulos, V., et al. (2013). Empirical modeling of plasma sheet pressure and three-dimensional force-balanced magnetospheric magnetic field structure: 1. Observation. *Journal of Geophysical Research: Space Physics*, *118*, 6154–6165. https://doi.org/10.1002/jgra.50585

Weimer, D. R. (2004). Correction to "Predicting interplanetary magnetic field (IMF) propagation delay times using the minimum variance technique". *Journal of Geophysical Research*, *109*, A12104. https://doi.org/10.1029/2004JA010691

Weimer, D. R., Ober, D. M., Maynard, N. C., Collier, M. R., McComas, D. J., Ness, N. F., et al. (2003). Predicting interplanetary magnetic field (IMF) propagation delay times using the minimum variance technique. *Journal of Geophysical Research*, *108*(A1), 1026. https://doi.org/10.1029/2002JA009405

Weygand, J. M., & McPherron, R. L. (2006a). *Wind 3DP Weimer propagated 60 s resolution in GSM coordinates*. https://doi.org/10.21978/P82K7X

Weygand, J. M., & McPherron, R. L. (2006b). *Wind Weimer propagated 60 s resolution tri-axial fluxgate magnetometer in GSM coordinates*. https://doi.org/10.21978/P8FW5P

Yue, C., Nishimura, Y., Lyons, L. R., Angelopoulos, V., Donovan, E. F., Shi, Q., et al. (2013). Coordinated THEMIS spacecraft and all-sky imager observations of interplanetary shock effects on plasma sheet flow bursts, poleward boundary intensifications, and streamers. *Journal of Geophysical Research: Space Physics*, *118*, 3346–3356. https://doi.org/10.1002/jgra.50372

Zesta, E., Singer, H. J., Lummerzheim, D., Russell, C. T., Lyons, L. R., & Brittnacher, M. J. (2000). The effect of the January 10, 1997, pressure pulse on the magnetosphere-ionosphere current system. In S. Ohtani, R. Fujii, M. Hesse, & R. L. Lysak (Eds.), *Magnetospheric current systems, geophys. Monogr. Ser* (Vol. 118, pp. 217–226). Washington, D.C: American Geophysical Union. https://doi.org/10.1029/gm118p0217

Zhou, X., Zhou, X.-Z., Angelopoulos, V., Shi, Q., Wang, C.-P., & Frey, H. (2013). Interplanetary shock–induced current sheet disturbances leading to auroral activations: THEMIS observations. *Journal of Geophysical Research: Space Physics*, *118*, 3173–3187. https://doi.org/10.1002/jgra.50175

Zhou, X.-Y., & Tsurutani, B. T. (2002). Interplanetary shock effects on the nightside auroral zone, magnetosphere and ionosphere. In *Proceedings of COSPAR colloquium on space weather study using multi-point TechniquesLing-hsiao lyu*. (Vol. 12, pp. 139–147). Elsevier. https://doi.org/10.1016/s0964-2749(02)80213-x